

How can existing ground-based profiling instruments improve European weather forecasts?

Article

Accepted Version

Illingworth, A. J., Cimini, D., Haefele, A., Haeffelin, M., Hervo, M., Kotthaus, S., Löhnert, U., Martinet, P., Mattis, I., O'Connor, E. J. and Potthast, R. (2019) How can existing ground-based profiling instruments improve European weather forecasts? *Bulletin of the American Meteorological Society*. pp. 605-619. ISSN 0003-0007 doi: <https://doi.org/10.1175/BAMS-D-17-0231.1> Available at <http://centaur.reading.ac.uk/82250/>

It is advisable to refer to the publisher's version if you intend to cite from the work. See [Guidance on citing](#).

To link to this article DOI: <http://dx.doi.org/10.1175/BAMS-D-17-0231.1>

Publisher: American Meteorological Society

All outputs in CentAUR are protected by Intellectual Property Rights law, including copyright law. Copyright and IPR is retained by the creators or other copyright holders. Terms and conditions for use of this material are defined in the [End User Agreement](#).

www.reading.ac.uk/centaur

CentAUR

Central Archive at the University of Reading

Reading's research outputs online



AMERICAN METEOROLOGICAL SOCIETY

Bulletin of the American Meteorological Society

EARLY ONLINE RELEASE

This is a preliminary PDF of the author-produced manuscript that has been peer-reviewed and accepted for publication. Since it is being posted so soon after acceptance, it has not yet been copyedited, formatted, or processed by AMS Publications. This preliminary version of the manuscript may be downloaded, distributed, and cited, but please be aware that there will be visual differences and possibly some content differences between this version and the final published version.

The DOI for this manuscript is doi: 10.1175/BAMS-D-17-0231.1

The final published version of this manuscript will replace the preliminary version at the above DOI once it is available.

If you would like to cite this EOR in a separate work, please use the following full citation:

Illingworth, A., D. Cimini, A. Haefele, M. Haeffelin, M. Hervo, S. Kotthaus, U. Löhnert, P. Martinet, I. Mattis, E. O'Connor, and R. Potthast, 2018: How can Existing Ground-Based Profiling Instruments Improve European Weather Forecasts?. *Bull. Amer. Meteor. Soc.* doi:10.1175/BAMS-D-17-0231.1, in press.

© 2018 American Meteorological Society



1 How can Existing Ground-Based Profiling Instruments
2 Improve European Weather Forecasts?
3

4 Authors:

5 A. J. Illingworth^{*1}, D. Cimini², A. Haeferle³, M. Haeffelin⁴, M. Hervo³, S. Kotthaus⁴, U.
6 Löhnert⁵, P. Martinet⁶, I. Mattis⁷, E. J. O'Connor⁸, and R. Potthast⁹

8 Affiliations:

9 ¹Department of Meteorology, University of Reading, UK

10 ²CNR-IMAA, Potenza, Italy & CETEMPS, University of L'Aquila, Italy

11 ³MeteoSwiss, Payerne, Switzerland

12 ⁴Institut Pierre Simon Laplace, Ecole Polytechnique, Palaiseau, France

13 ⁵Institute for Geophysics and Meteorology, University of Cologne, Germany

14 ⁶CNRM UMR 3589, Meteo France/CNRS, Toulouse, France

15 ⁷Deutscher Wetterdienst, Observatorium Hohenpeißenberg, Germany

16 ⁸Finnish Meteorological Institute, Finland

17 ⁹Deutscher Wetterdienst, Offenbach, Germany

18
19 * *Corresponding author address:* Anthony J. Illingworth, Department of Meteorology,
20 University of Reading, Earley Gate, PO Box 243, Reading RG6 6BB, UK

21 Tel: +44 118 378 6508 E-mail: a.j.illingworth@reading.ac.uk

22
23 ABSTRACT

24 To realise the promise of improved predictions of hazardous weather such as flash floods, wind
25 storms, fog and poor air quality from high-resolution mesoscale models, the forecast models

26 must be initialized with an accurate representation of the current state of the atmosphere, but
27 the lowest few km are hardly accessible by satellite, especially in dynamically-active
28 conditions. We report on recent European developments in the exploitation of existing ground-
29 based profiling instruments so that they are networked and able to send data in real-time to
30 forecast centers. The three classes of instruments are: (i) Automatic lidars and ceilometers
31 providing backscatter profiles of clouds, aerosols, dust, fog and volcanic ash, the last two being
32 especially important for air traffic control; (ii) Doppler wind lidars deriving profiles of wind,
33 turbulence, wind shear, wind-gusts and low-level jets; and (iii) Microwave radiometers
34 estimating profiles of temperature and humidity in nearly all weather conditions. Twenty-two
35 European countries and fifteen European National Weather Services are collaborating in the
36 project, that involves the implementation of common operating procedures, instrument
37 calibrations, data formats and retrieval algorithms. Currently, data from 220 ceilometers in 17
38 countries are being distributed in near real-time to national weather forecast centers; this should
39 soon rise to many hundreds. The wind lidars should start delivering real time data in late 2018,
40 and the plan is to incorporate the microwave radiometers in 2019. Initial data assimilation tests
41 indicate a positive impact of the new data.

42

43 CAPSULE

44 Observations of profiles of winds, aerosol, clouds, winds, temperature and humidity in the
45 lowest few km of the atmosphere from networks of ceilometers, Doppler wind lidars and
46 microwave radiometers are starting to flow in real time to forecasting centers in Europe.

47

48 The high-resolution (1 km) forecasting models that are now run operationally by many
49 European National Weather Services promise to provide increasingly accurate high-resolution
50 forecasts of impending hazardous weather, ranging from flash floods to episodes of poor air

51 quality. The WMO guidance for NWP applications highlights the need for wind, temperature
52 and humidity profiles, especially in cloudy areas¹. Satellites can provide data in the upper
53 troposphere, but if this promise is to be fulfilled, in particular for short-range forecasts, a new
54 generation of high-density observations through the lower few km of the atmosphere, including
55 the boundary layer, is required in real-time. This region close to the ground is particularly
56 difficult to observe with satellites due to the frequent occurrence of clouds and, for passive
57 instruments, the broad weighting functions and the effects of the variable albedo or brightness
58 temperature of the surface.

59

60 Illingworth et al. (2015) noted the potential of ground-based networks of automatic low-power
61 backscatter lidars/ceilometers (ALC)², Doppler Wind Lidars (DWL) and Microwave
62 Radiometers (MWR) to supply real-time observation to forecast centers. In this paper we report
63 recent developments in the exploitation of these networks. Observations of profiles of aerosols,
64 clouds, winds, temperature and humidity in the lowest few km of the atmosphere in Europe are
65 now starting to flow in real time to forecasting centers. This has been achieved as a result of
66 collaboration between a COST action (see sidebar) ‘TOPROF: Towards operational ground-
67 based profiling with ALCs, DWL and MWRs for improving weather forecasts’
68 (www.cost.eu/COST_Actions/essem/ES1303) and EUMETNET, an organization which
69 provides a framework to enable the European Weather Services to work together, share ideas,
70 best practice and to share the cost of major infrastructure investments. The EUMETNET
71 Composite Observing System (EUCOS) is responsible for developing an observing system for

¹ See WMO statements of guidance for high-resolution and global NWP at:
<https://www.wmo.int/pages/prog/www/OSY/SOG/SoG-HighRes-NWP.pdf>
<https://www.wmo.int/pages/prog/www/OSY/SOG/SoG-Global-NWP.pdf>

² Ceilometers were originally conceived to measure cloud base altitude only, but today the sensitivity of these instruments is sufficient to provide profiles of backscattered power from aerosols and clouds. Hence a new terminology has been proposed that combines automatic low-power lidars and ceilometers into ALCs.

72 Europe serving the needs of regional numerical weather prediction (NWP). One of
73 EUMETNET's programs is 'E-PROFILE' that originally involved only radar wind profilers,
74 but has been extended to include ALC networks and more recently is incorporating DWLs with
75 a projected extension to distribute MWR data. The TOPROF action ran from October 2013 to
76 October 2017 with financial support from the European Union and was responsible for setting
77 up common calibration techniques, operating procedures, deriving error characteristics,
78 developing retrieval algorithms, and ensuring homogeneous and reliable data quality for the
79 three classes of instruments, whereas EUMETNET through its E-PROFILE program is
80 involved in the networking and near real-time distribution of observations to the national
81 weather services.

82

83 The ALCs under investigation in the E-PROFILE network transmit short pulses of laser
84 radiation with wavelengths 532, ~ 910 or 1064 nm and receive a backscattered signal with a
85 delay that provides range information. The raw data are averaged to 15-30m vertical resolution
86 and 15-60 seconds in time. Examples of the use of attenuated backscatter profiles include
87 characterising clouds, aerosols, dust, fog and volcanic ash as discussed in more detail in the
88 ALC section, the last two being especially important for air traffic control. At present,
89 attenuated backscatter profiles from over 220 ALCs in 17 countries are being distributed by
90 EUMETNET E-PROFILE in near real-time to National Weather Services and can be viewed
91 at <http://eumetnet.eu/e-profile/>, (Wiegner et al. 2014). These data are homogenized and
92 calibrated using the developments carried out in TOPROF.

93

94 Fig. 1 represents the map of E-PROFILE stations in green and stations that will be integrated
95 before the end of 2018 in blue: ALCs that are present in Europe but not yet integrated into E-
96 PROFILE are in red (data from DWDs ceilomap <https://www.dwd.de/ceilomap>). In June 2018,

97 the Saddleworth Moor fire near Manchester injected large quantities of smoke into the
98 atmosphere. This smoke was transported over UK and Europe and measured by the E-
99 PROFILE network. The measurements from 26 to 28 June at five E-PROFILE stations are
100 displayed in Fig. 1. Aerosol layers are visible in the free troposphere (at altitudes between 2
101 and 5 km). Measurements above thick clouds (represented with black dots) appear as white
102 vertical stripes because the laser beam is fully attenuated. These measurements are also visible
103 on the E-PROFILE website and clearly illustrate the capabilities of the network in monitoring
104 aerosol layers over Europe.

105

106 In contrast to ALCs which have been in use for many years, DWLs have undergone recent
107 development using solid-state fibre-optic technology at a wavelength of $\sim 1.5 \mu\text{m}$. The type of
108 DWL being incorporated into the E-PROFILE network obtains the radial Doppler shift of the
109 backscattered signal from aerosol or cloud particles in the direction of the beam using the high
110 pulse rate heterodyne technique. From the radial Doppler velocities, the vertical structure of
111 winds, wind shear, levels of turbulence, inference of the maximum gusts, properties of low-
112 level jets and classification of the state of the boundary layer can be obtained. The minimum
113 range is typically 50-90 m, with the maximum range varying from 2-10 km; in practice the
114 sensitivity of most instruments usually limits the observations to within the boundary layer
115 where there are sufficient aerosols. Wind measurements are not possible inside or above
116 optically thick clouds or in heavy rain.

117

118 Ground-based microwave radiometers (MWR) measure the natural down-welling thermal
119 emission in the microwave part of the electromagnetic spectrum originating from Earth's
120 atmosphere and the cosmic background. The radiance observations are commonly expressed
121 as an equivalent brightness temperature (T_B) from which estimates of atmospheric temperature

122 profiles (from oxygen absorption from 55 to 60 GHz) and humidity profiles (from water vapor
123 absorption around 22 GHz) as well as column-integrated water vapor (IWV) and liquid water
124 path (LWP) can be inferred during non-precipitating conditions. Valid temperature profiles can
125 also be inferred in the presence of low-moderate precipitation. The MWR profiling capability
126 in the lowest 2 km of the atmosphere is proving to be valuable because of the poor sampling
127 by other sensors (e.g. from satellite).

128

129 All these instruments are rugged and can operate autonomously for long periods requiring little
130 maintenance and do not need specialised staff, but how can these new observations contribute
131 to NWP? Firstly, they can be used to check that the parameterisation schemes inherent in such
132 models lead to a realistic representation of the current state of the atmosphere. For more than
133 ten years the Cloudnet project (Illingworth et al. 2007) has used vertically pointing cloud
134 radars, ACLs and MWRs to derive cloud properties, compared them with the representation of
135 clouds within several operational European forecast models and produced statistics of the
136 model performance (<http://cloudnet.fmi.fi>). In Cloudnet the ALCs were only used to identify
137 cloud base of liquid clouds and the MWRs to derive their liquid water path. A more rigorous
138 approach is to compare the observations ('O') with their representation in the model (the
139 background 'B') to obtain the 'O-B' statistics and to check that any biases are sufficiently small
140 and, ideally, that the errors are Gaussian. This procedure is fairly straightforward for the winds
141 from a DWL because the model has a prognostic wind variable. This is not the case for the
142 ALC backscatter signal nor for the brightness temperature from microwave radiometers, so a
143 '*forward model*' must be used that operates on the prognostic variables within the NWP model
144 to predict the value of the observed parameter which can then be directly compared with the
145 observation. Once the O-B statistics are deemed to be acceptable then there is potential for
146 *data assimilation* whereby the initial state of the model is updated with the observations

147 accounting for the errors in both the observations and the model, so that the NWP model can
148 be initialised with the best possible representation of the current state of the atmosphere. A
149 more accurate initial state usually reduces the errors in the forecast.

150

151 If the new observations are to be useful, then it is essential that the data are calibrated and
152 unbiased and the quality is homogeneous with known error characteristics. TOPROF's major
153 tasks have been to establish common calibration procedures for the three classes of instruments,
154 common checks on data quality, and independent validation of the veracity of the data.
155 TOPROF has also developed forward models for predicting the ALC and MWR observations
156 from the NWP representation, and defined common data formats and protocols for transmitting
157 the data to a central hub from where they can be distributed to the national weather services.
158 Finally, TOPROF has started gathering O-B statistics of model performance and carried out
159 some simple data assimilation trials that indicate a positive impact on the forecast.

160

161 **AUTOMATIC LOW-POWER LIDARS AND CEILOMETERS (ALCS).**

162 Figure 2 shows a warm front crossing Germany in the morning of 25 August 2018 as observed
163 at Ulm by a CHM15-k ceilometer of the DWD network. The cloud base height descended from
164 10 km at midnight to 2.5 km at 0800 UTC. Rain started at 0900 UTC, visible as red vertical
165 stripes between the cloud base and the ground. The yellowish horizontal line at 2 km altitude
166 between 1200 and 1500 UTC shows the melting layer (dark band). After the frontal passage
167 (at about 1500 UTC), the steady rain stopped and the stratiform clouds were replaced by broken
168 cumulus, with some precipitation below cloud base that occasionally reached the ground.
169 Liquid water clouds can be identified by a thin layer with very high backscatter at cloud base
170 followed by rapid extinction of the ceilometer signal, for example near heights of 2-3 km at
171 0000, 0200 and from 1700 - 2100 UTC, whereas the ceilometer signal penetrates further into

172 ice clouds. Before the frontal passage the planetary boundary layer (PBL) was characterized
173 by a significant aerosol load with backscatter values $> 1 \text{ Mm}^{-1} \text{ sr}^{-1}$ up to ~ 2 km height, but was
174 cleaner during the afternoon; this could be due to wash-out or a different, cleaner air mass. Note
175 the two thin aerosol layers from long range transport (in yellow) at 8 and 10.5 km altitude after
176 2200 UTC with backscatter values $\sim 0.5 \text{ Mm}^{-1} \text{ sr}^{-1}$, possibly from forest fires in North America.

177

178 Three classes of ALCs are being used in the E-PROFILE network. CL31 and CL51 from
179 Vaisala measuring at ~ 910 nm, CHM15k from Lufft measuring at 1064 nm and Mini-MPL
180 from Sigma-Space, measuring at 532 nm. Other ALCs are also exploited at some sites such as,
181 for example, the CS135 from Campbell Scientific (910 nm) or the CE370 from CIMEL (532
182 nm). ALCs are characterized by their continuous 24-7 operation capabilities with high
183 sampling rates. In the low-altitude range, the optical overlap between the emitting (laser) and
184 receiving (telescope) optical components of an ALC changes with altitude. If this overlap
185 function is not well characterized, exploitation of the measurements at low-altitude may be
186 restricted. In the far-altitude range, the signal-to-noise ratio may limit the exploitation of the
187 measurements for detecting low-scattering media such as aerosols. Some more sensitive
188 systems may, on the contrary, suffer from saturation due to high-scattering media such as liquid
189 water clouds at short range. Some of these effects can be corrected to improve signal quality.
190 All ALCs must also be calibrated in order to derive quantitatively meaningful attenuated
191 backscatter profiles that can be compared from one instrument to the next and with values
192 predicted from NWP forward models.

193

194 a) *Determining optical overlap functions.* The optical design of CL31 (CL51) instruments yield
195 a complete overlap around 50m (200m) (e.g. Haeffelin et al. 2012; Wiegner et al. 2014). The
196 bi-axial lidars like CHM15k or Mini-MPL reach complete optical overlap around 1km with

197 very noisy signal below 150-200 m, a region where the optical overlap is close to zero. Hervo
198 et al. (2016) found that the optical overlap function of the CHM15k is affected by temperature
199 fluctuations. They developed a methodology to determine the temperature dependence and
200 correct for it, yielding a precise attenuated backscatter values in the partial overlap region.

201 b) *Correcting signal artifacts.* Kotthaus et al. (2016) found signal artifacts in the free
202 troposphere in CL31 attenuated backscatter profiles, characterized by negative values in cloud-
203 free regions due to a shift of the raw data introduced by the system firmware, and developed a
204 method to quantify these artifacts and correct for them. These results convinced Vaisala to
205 release a new firmware for TOPROF that removes the artificial shifts to allow more
206 quantitative exploitation of the CL31 attenuated backscatter profiles;

207 c) *ALC Calibration.* The signal detected by the ceilometers must be converted into an absolute
208 value of backscatter measured in units of $\text{m}^{-1} \text{sr}^{-1}$. This is best accomplished by using a
209 reference target whose backscatter characteristics are known. One approach uses the known
210 integrated backscatter for a water cloud that total extinguishes the ceilometer signal; this can
211 be obtained by adding the observed backscatter at each gate within the cloud, and adjusting the
212 ceilometer calibration until this integral, after correction for multiple scattering, is equal to
213 0.027 m^{-1} . For details see O'Connor et al. (2004). Hopkins et al. (submitted to AMT) showed
214 that this calibration is accurate to better than 10% with no significant annual variation. A second
215 approach for photon-counting instruments measuring at 532 nm or, more commonly at 1064 nm,
216 is to use the molecular return as a reference because it is a function of the known air density
217 (Fernald et al. 1972; Klett, 1985; Wiegner and Geiß, 2012; Baars et al. 2016). The molecular
218 return at 1064 nm is small, but photon counting instruments are able to measure it with
219 sufficiently long averaging times (Wiegner and Geiß, 2012) and Fig. A2 in Baars et al. (2016).
220 The method developed within TOPROF relies on averaging the backscatter return for 6
221 hours on a clear night; sensitivity studies showed that typical accuracies of the calibration are

222 of the order of 10%-15%. The calibrations can be up to a factor of two different from those
223 supplied by the manufacturer. These two methods are implemented by E-PROFILE to
224 distribute calibrated attenuated backscatter data to national weather services. Wiegner and
225 Gasteiger (2015) propose a method to correct for water vapor absorption for ALC
226 measurements that operate at wavelengths affected by this effect (e.g. 905-910 nm).

227 d) *ALC measurement uncertainties for Lufft and Vaisala due to incomplete optical overlap,*
228 *signal artifacts, and calibration.* These have been estimated using data from a three-month
229 experiment ‘CEILINEX’ when 12 ALCs were operated side-by-side (<https://ceilinex2015.de/>,
230 Pattantyús-Ábrahám et al. 2017). Fig. 3 shows a comparison of raw ALC signal and calibrated
231 attenuated backscatter signal from 8 co-located ALCs including Campbell Scientific, Vaisala,
232 and Lufft instruments based on 3 hours of data on 13 Aug 2015. The profiles show a stable
233 nocturnal boundary layer up to 300 m and a residual layer up to 750 m. Additionally, there are
234 two lofted aerosol layers (probably Saharan dust) between 1 and 4 km. Fig. 3 shows that
235 differences less than 25% can be expected for calibrated attenuated backscatter, in particular
236 for altitudes greater than 500 m. Below 500 m the greater differences between the Lufft and
237 Vaisala instruments can be attributed to systematic errors in the overlap function correction.
238 Note also inconsistencies below 250 m between CL31 and CL51 profiles and between the
239 different Lufft ALCs, confirming that data should be used with great care at such low altitudes.
240 CL31 and CL51 measurements have a lower signal-to-noise ratio than the other instruments at
241 altitudes greater than 1000 m and so are less sensitive for monitoring lofted aerosol.

242

243 Applications using ALC measurements are numerous. Several studies were conducted in the
244 framework of the TOPROF action that resulted in the evaluation of aerosols in atmospheric
245 models based on ALC forward models and O-B statistics (e.g. Warren et al. 2018), providing
246 diagnostics of the atmospheric boundary layer height (Lotteraner and Piringer 2016; Poltera et

247 al. 2017; Kotthaus and Grimmond, 2018), supporting warning of fog formation (Haeffelin et
248 al. 2016), and detecting transport of dust, biomass burning and volcanic ash (Cazorla et al.
249 2017; Roman et al. 2018). Fig. 4 shows an example of comparisons between attenuated
250 backscatter observed by an ALC and modeled using the ECMWF CAMS forward model³. The
251 observations were performed by a CHM15k in Valladolid and calibrated using the
252 methodology described above. Saharan dust aerosols are clearly visible up to 5 km, both in the
253 observations and the forecasts. The mean bias for this event is lower than 5%, showing the
254 good agreement between observations and forecasts. Chan et al. (2018) carried out a year- long
255 comparison of the representation of aerosols within the CAMS model and from the German
256 ceilometer network and found very good agreement with the arrival time and vertical extent of
257 a Saharan dust layer. Fig. 5 shows an example of low-altitude ALC-derived information during
258 3 hours in pre-fog conditions at the Charles-de-Gaulle airport near Paris. The bottom panel
259 shows the 0-400 m ALC attenuated backscatter profile, while the top panel provides fog alerts
260 based on Haeffelin et al. (2016). At 0430h, more than 1 hour before the first alerts, the sky is
261 cloud free (bottom panel) favoring radiative cooling and the ALC backscatter is quite high
262 between 50-150 m, revealing the presence of large aerosols in a moist atmosphere. At 0550h,
263 a cloud forms about 100 m agl generating severe-level alerts aloft, and rapidly subsides to the
264 ground, leading to persistent fog after 0645h, about 1 hour after the first severe-level alerts.

265

266 **DOPPLER WIND LIDARS (DWLs)**

267 The Doppler lidar instruments considered by the TOPROF action were those with sufficient
268 sensitivity and a scanning capability so that the horizontal wind profile could be derived
269 throughout the boundary layer. These included instruments from Halo Photonics (Streamline,

³ Developed for the CALIOP lidar data from CALIPSO satellite in the A-train, (Benedetti et al., 2009) but looking upwards instead of downwards. The model carries aerosol type and size and so the optical depth/extinction is calculated, and the assumed lidar ratio converts extinction into the observed value of backscatter.

270 Streamline Pro and Streamline XR) and Leosphere (WindCube 100S, 200S and 400S), all
271 configurable to have a maximum range of about 10 km and range resolution of 50 m or better.
272 All DWL considered in TOPROF are full-hemispheric scanning, except for the Halo Photonics
273 Streamline Pro, which can scan within a cone from 70° above the horizon to zenith and has no
274 external moving parts. One task in TOPROF was to design suitable scanning strategies
275 optimized to extract as much information as possible. The scanning capability is utilized to
276 reconstruct the vertical profile of the horizontal wind from the measured radial components.
277 This can be performed in a similar manner as for radar wind profilers by means of ‘Doppler
278 Beam Swinging’ where the wind speed and direction are derived from the radial (line-of-sight)
279 components from off-zenith dwells at different azimuths, or by using a conical Velocity-
280 Azimuth-Display (VAD) scan where the wind speed and direction can be inferred from the
281 magnitude and phase of the sinusoidal azimuthal variation of the observed radial component
282 of the wind. Both methods rely on assuming horizontal homogeneity in order to derive the
283 horizontal component; this may not be applicable in strongly turbulent situations, or in flows
284 over complex terrain. TOPROF recommends performing a VAD scan with a minimum of 12
285 beams, and, using the method of Päsche et al. (2015), which, in addition to generating the
286 horizontal wind profile, provides a metric describing the likelihood of inhomogeneity
287 degrading the retrieval. Teschke and Lehmann (2017) note that the optimal elevation angle for
288 a VAD scan is about 35° from horizontal but that this is not a strong constraint; suitable
289 elevation angles for VAD scanning lie between 15° and 70° from horizontal. Hence, TOPOROF
290 recommends performing two VAD scans; a primary scan at high elevation ($50\text{-}70^\circ$ from
291 horizontal) to capture the wind profile to the top of the boundary layer; and a rapid low-
292 elevation scan at 15° or lower in elevation (dependent on local obstructions), from which the
293 vertical profile can be extended down towards the surface below the minimum altitude probed
294 by the higher elevation scan. The inclusion of an additional scan at a low elevation can also be

295 used to investigate the spatial representativeness of the wind profile.

296

297 Such high vertical resolution wind profiles are ideal for capturing the presence of wind shear,
298 and low-level jets, an important consideration for wind energy, aviation, and air quality
299 applications. An objective method for diagnosing low-level jets was developed (Tuononen et
300 al., 2017) and is now being implemented routinely at a number of sites (Marke et al., 2018).
301 Vertical dwells with high temporal resolution (5 seconds or better) within the VAD scans allow
302 the retrieval of turbulent parameters such as vertical velocity variance, skewness and
303 dissipation rate of turbulent kinetic energy (O'Connor et al., 2010). Combining these
304 parameters permits a classification of the atmospheric boundary layer structure (Manninen et
305 al, 2018) in which the turbulent regions are detected, and a probable source of turbulence
306 assigned: e.g. whether wind shear or buoyancy production dominates, or whether convection
307 is surface-driven or cloud-driven. The classification scheme also notes whether the turbulent
308 layers are in contact with the surface, an important distinction when calculating dispersion in
309 chemical transport models. Turbulent parameters can also be derived from VAD scans
310 (Vakkari et al., 2015), reconstructed using a stochastic particle filter (Rottner et al., 2017), and
311 the combination of winds and turbulence can be used to diagnose wind gusts (Suomi et al.,
312 2017) especially important in forecasting and assessing wind-induced damage.

313

314 DWL products can be used to validate the boundary layer schemes employed in forecast
315 models, even in challenging locations (a coastal example is given in Fig. 6), and to evaluate
316 the much more spatially dense ALC retrievals (Schween et al. 2014). Generating these new
317 products routinely requires that DWL uncertainties are known and well characterized. Known
318 hard targets such as towers and masts can be used to check the radial Doppler velocity, and that
319 the pointing angle is correct. Azimuthal pointing repeatability for these instruments was shown

320 to be excellent, typically within 0.25° . Uncertainties in radial Doppler velocity estimates are a
321 function of the number of pulses sampled and their signal-to-noise ratio (SNR). TOPROF
322 worked together with the manufacturers on understanding and improving the data processing
323 to yield reliable data. Reducing the median bias in SNR to about 0.0002 led to improvements
324 in sensitivity by as much as a factor of 5 to 10 (Manninen et al. 2016), so that a lower SNR
325 threshold could be used to diagnose 'good' data. The bias reduction permits more reliable
326 uncertainty estimates, yielding more accurate turbulent parameters. Long-term comparisons of
327 the resulting wind estimates compare very well with masts and other measurements at high
328 SNR with root mean squared errors, RMSE, of $< 0.7 \text{ m s}^{-1}$ for wind speed and $< 10^\circ$ for
329 direction (e.g. Päsche et al. 2015), but care should be taken when calculating wind
330 climatologies in low SNR conditions (Gryning et al. 2016). Now that the data quality has been
331 established the next step is to establish the O-B statistics. In principle, DWLs provide profiles
332 of attenuated backscatter similar to ALCs. DWLs operating with a telescope focused at infinity
333 can use the same liquid cloud method as for ALCs (Westbrook et al. 2010) for calibrating the
334 backscatter power. However, by adjusting the telescope focus, extra sensitivity in the BL can
335 be achieved while sacrificing sensitivity in the far range; beneficial for retrieving winds and
336 turbulence in the boundary layer, but more difficult to account for in calculating the profile of
337 attenuated backscatter. Extensive comparisons with instrumented towers confirm the accuracy
338 of the winds derived from DWLs and a more comprehensive O-B comparison is planned using
339 the two-year data set obtained from the DWL network.

340

341

342 **MICROWAVE RADIOMETERS (MWRs)**

343 MWR measure downwelling radiation in terms of atmospheric brightness temperatures (T_B)
344 that are then converted to atmospheric variables of interest. TOPROF fostered breakthrough

345 developments in both MWR hardware and software leading to more accurate T_B observations,
346 relevant for direct data assimilation, and also to improved retrievals of atmospheric variables.
347 The instruments considered here are multi-channel temperature and humidity profilers
348 operating in the 22-31 (humidity) and 51-60 (temperature) GHz bands, such as Radiometer
349 Physics (RPG)⁴ HATPRO and Radiometrics MP3000⁵ (Ware et al. 2003; Rose et al. 2005; De
350 Angelis et al. 2017). These instruments also provide the column-integrated amount of water
351 vapor (IWV) and cloud liquid water path (LWP).

352

353 Two Joint Calibration (JCAL) field experiments were organized in cooperation with leading
354 MWR manufacturers, triggering the development of new calibration targets and receiver
355 technology. RPG has developed a new arrangement for the liquid nitrogen calibration target
356 that eliminates calibration uncertainties due to reflections and standing waves and provides
357 absolute accuracies of T_B on the order of 0.1 K, which is a factor ~ 5 more accurate than
358 previous targets. The load was introduced with the 5th HATPRO generation, which also
359 includes an improved receiver technology resulting in T_B noise levels also on the order of 0.1
360 K at 1 s temporal resolution. Czekala (personal communication) has shown that this can lead
361 to an uncertainty reduction of the temperature profile retrieval by up to 0.3 K, leading to more
362 reliable detection of temperature inversions in the boundary layer. These hardware
363 developments can also improve the accuracy of IWV and LWP retrievals by up to 50%. The
364 new calibration load is also compatible with radiometers of older generations.
365 Recommendations for operational calibration, measurement and quality procedures suited for
366 network operation were agreed upon and distributed
367 (<http://cetemps.aquila.infn.it/mwrnet/reports.html>). In addition, a software package for data

⁴<https://www.radiometer-physics.de/products/microwave-remote-sensing-instruments/radiometers/humidity-and-temperature-profilers/>

⁵<http://radiometrics.com/mp-series/>

368 post-processing including retrieval application, quick-look generation, and output conversion
369 (compliant with the Climate and Forecast metadata convention) for most common MWR types
370 is available (http://cetemps.aquila.infn.it/mwrnet/mwr_pro.html).

371

372 A fast forward model has been developed (De Angelis et al. 2016) by adapting existing
373 software widely used for satellite data assimilation so that it can calculate the downwelling T_B s
374 that would be observed at the ground and their Jacobians from any source of atmospheric
375 temperature and humidity profiles (e.g. radiosondes or an NWP model). The software,
376 RTTOV-gb, (<http://cetemps.aquila.infn.it/mwrnet/rttovgb.html>), is freely available, and
377 validation with a reference line-by-line (LBL) computation shows unbiased rms differences
378 within 0.2 K, so the error of the parametrized forward model is within the instrumental
379 uncertainty. In order to monitor the behavior of continuous T_B observations, O-B statistics were
380 computed for a 1-year dataset from a prototype network of six MWRs (De Angelis et al. 2017).
381 Within this network standardized calibrations procedures and data life cycle had been
382 implemented so that quality-controlled data were collected. The six prototype network stations
383 are located at: Cabauw, NL (51.97N/4.93E), Jülich, GER (50.91N/6.41E), Leipzig, GER
384 (51.35N/12.43E), Lindenberg, GER (52.21N/14.12E), Palaiseau, FRA (48.40N/2.36E), and
385 Payerne, SUI (46.82N/6.95E). Fig. 7 shows the 1-year time series of O-B comparison at one
386 site for four frequency channels. The NWP model used here is AROME, Application of
387 Research to Operations at Mesoscale, developed by Météo-France (Seity et al. 2011).

388

389 The O-B analysis revealed that typical differences are within the expected total uncertainty and
390 that the O-B distributions were Gaussian, confirming their suitability for variational data
391 assimilation. The analysis also demonstrated how such monitoring is able to detect an
392 instrument malfunction leading to a mis-calibration and then to verify that a re-calibration has

393 been successful as described in Fig. 7. The O-B analysis showed consistent characteristics over
394 time and instrument site/type with a typical O-B bias for well-maintained instruments being
395 generally below 1K, but reaching ~3K at lower frequency oxygen channels, where the forward
396 model uncertainty reaches its maximum (De Angelis et al. 2017; Cimini et al. 2018). However,
397 even these uncertainties can be effectively addressed because the biases were persistent and the
398 random component was similar throughout the prototype network. The uncertainty of the
399 reference LBL calculations have also been investigated (Cimini et al. 2018), possibly
400 explaining systematic O-B differences exceeding 1 K that must be accounted for within a bias
401 correction scheme. A platform for continuously monitoring O-B quick-looks in near-real-time
402 is up and running and available for all interested users ([https://tinyurl.com/MWR-O-B-](https://tinyurl.com/MWR-O-B-JOYCE)
403 [JOYCE](https://tinyurl.com/MWR-O-B-JOYCE)). The main goal of this platform is i) to provide an independent instrument performance
404 monitoring tool for MWR operators and ii) to attest the suitability of MWR for operational use
405 by National Weather Services.

406
407 In addition to the prototype network, there are some 30 MWR stations over Europe that have
408 the potential to deliver TBs and derived products on a continuous basis. Details of the network
409 can be found at <http://cetemps.aquila.infn.it/mwrnet/MWRnetmap.html>. Long data records
410 (exceeding 10 years) are available from some of these sites, in Europe (e.g. Lindenberg (GER),
411 Payerne (SUI), and Potenza (IT)) as well as in the USA (e.g. ARM sites; Cadeddu et al. 2013).
412 MWR data assimilation promises to be useful for adjusting NWP model temperature and
413 humidity fields of the lowest 2 km, especially in convective (Cimini et al. 2015) and very stable
414 conditions (Martinet et al. 2017). Fig. 8 shows how the assimilation of MWR brightness
415 temperatures leads to an improvement in the temperature analysis in an enclosed Alpine valley
416 during stable conditions where the true structure has been established from a series of
417 radiosonde ascents; the stability close to the ground is a crucial parameter in the build-up and

418 dispersion of pollutants. Similarly, Fig. 9 shows large potential improvements in both
419 temperature and humidity profiles when observations from one MWR are used to correct the
420 NWP forecast, in a so-called one-dimensional variational retrieval (1DVAR) scheme. 24-hour
421 time series of temperature and humidity profiles from a NWP forecast, 1DVAR retrievals, and
422 the analysis increment are shown. Based on these results, Météo-France decided to deploy a
423 MWR network for an international fog field campaign planned for Dec 2019-Feb 2020 (four
424 to six MWR units in a 300x200 km domain). Forecast indices derived from MWR observations
425 were also demonstrated to be useful in support of nowcasting and short-range weather
426 forecasting (Cimini et al. 2015). Continental-scale data assimilation trials show positive-to-
427 neutral impact, especially for accumulations of precipitation up to 18h after forecast
428 initialization (Caumont et al. 2016). The impact of MWR-derived thermodynamic profiles is
429 larger when they are used to substitute classical radiosonde observations in a data denial
430 experiment. Data assimilation results obtained so far did not take advantage of the recent
431 hardware and software developments, so there is clearly potential for improvement.

432

433 **CONCLUSIONS**

434 Networks of ground-based profiling instruments with improved retrieval algorithms and
435 standardized software and calibration procedures have been developed by TOPROF in
436 collaboration with instrument manufacturers and implemented by the E-PROFILE program of
437 the EUMETNET consortium of European National Weather Services. These networks are
438 providing an increased understanding of process within the lowest few km of the atmosphere,
439 and, ultimately, have the potential for assimilation into operational NWP models.
440 Improvements have been made in the Automatic Lidar and Ceilometer (ALC) algorithms that
441 correct for overlap, remove artifacts in the profiles, and provide absolute backscatter calibration
442 to within ~10% using natural targets as a reference; either the integrated backscatter from thick

443 water clouds or the molecular return. The network has the demonstrated capability for tracking
444 smoke from forest fires and desert dust, issuing fog formation warnings, and for providing
445 vertical profiles of cloud and aerosols. An O-B comparison of the observed backscatter from
446 desert dust with those from an ECMWF forward model indicates that biases are below 10%.
447 Profiles of aerosol and cloud backscatter from a network of 220 ALCs (as of September 2018)
448 are being distributed in real time to European weather forecast centers and this should increase
449 to several hundreds within the next year.

450

451 A network of Doppler Wind Lidars (DWLs) is being set up and test data are now being
452 distributed in experimental mode to forecast centers by E-PROFILE. DWLs use aerosol or
453 cloud particles as tracers of the line of sight component of atmospheric motion. Standardized
454 scanning procedures and algorithms have been established so they can routinely provide data
455 on wind profiles in the boundary layer with an rms accuracy of $< 10^\circ$ in direction and better
456 than 0.7 m s^{-1} in speed. These observations can be used for diagnosis of the existence of low-
457 level jets, deriving profiles of vertical velocity variance and skewness, and the dissipation rate
458 of turbulent kinetic energy. The combination of the wind and turbulence can be used to
459 diagnose wind gusts, needed for forecasting and assessing wind-induced damage, and for
460 classification of the atmospheric boundary layer structure so that those turbulent layers in
461 contact with the surface can be identified; this is an important property when calculating the
462 dispersion by chemical transport models.

463

464 TOPROF studies have led to advances in Microwave Radiometer (MWR) hardware and
465 software so the instruments can provide brightness temperature (T_B) calibrations to within
466 0.1K. A ground-based version of the RTTOV radiative transport model has been developed
467 and characterized, so that T_B and its uncertainty can be calculated from a forecast model. Tests

468 over one year comparing these forward modeled values of T_B with those observed with a
469 prototype network of six MWRs show that typical O-B biases for well-maintained instruments
470 are generally below 1K. Field campaigns have demonstrated that the assimilation of T_B into an
471 operational mesoscale model leads to improved temperature and humidity structure in the
472 lowest 2 km of the atmosphere. E-PROFILE is evaluating the extension of their activities to
473 MWR so that data can be distributed in real time to European weather forecast centers starting
474 from 2019.

475

476 **ACKNOWLEDGEMENTS**

477 This article/publication is based upon work from COST Action ES1303 ‘TOPROF’ supported
478 by COST (European Cooperation in Science and Technology, www.cost.eu).

479

480 **REFERENCES**

- 481 Baars, H. and Coauthors, 2016: An overview of the first decade of Polly^{NET}: an emerging
482 network of automated Raman-polarization lidars for continuous aerosol profiling. *Atmos.*
483 *Chem. Phys.*, **16**, 5111-5137. doi:10.5194/acp-16-5111-2016.
- 484 Benedetti, A. and Coauthors, 2009: Aerosol analysis and forecast in the European Centre for
485 Medium-Range Weather Forecasts Integrated Forecast System: 2. Data assimilation. *J.*
486 *Geophys. Res.*, **141** D13205. doi:10.1029/2008JD011115.
- 487 Cadeddu, M. P., Liljegren, J. C., and Turner, D. D., 2013: The Atmospheric radiation
488 measurement (ARM) program network of microwave radiometers: instrumentation, data,
489 and retrievals. *Atmos. Meas. Tech.*, **6**, 2359–2372, [https://doi.org/10.5194/amt-6-2359-](https://doi.org/10.5194/amt-6-2359-2013)
490 2013.

491 Caumont O., D., and Coauthors 2016: Assimilation of humidity and temperature observations
492 retrieved from ground-based microwave radiometers into a convective-scale model. *Q. J. R.*
493 *Meteorol. Soc.*, **142**: 2692–2704. doi:10.1002/qj.2860.

494 Cazorla, A., and Coauthors, 2017: Near-real-time processing of a ceilometer network assisted
495 with sun-photometer data: monitoring a dust outbreak over the Iberian Peninsula. *Atmos.*
496 *Chem. Phys.*, **17**, 11861–11876. <https://doi.org/10.5194/acp-17-11861-2017>.

497 Chan, K. L., and Coauthors, 2018: Evaluation of ECMWF-IFS (version 41R1) operational
498 model forecasts of aerosol transport by using ceilometer network measurements. *Geosci.*
499 *Model. Dev.*, **11**, 3807-3831. doi.org/10.5194/gmd-11-3807-2018.

500 Cimini, D., M. Nelson, J. Güldner, and R. Ware, 2015: Forecast indices from a ground-based
501 microwave radiometer for operational meteorology. *Atmos. Meas. Tech.*, **8**, 315-333,
502 <https://doi.org/10.5194/amt-8-315-2015>.

503 Cimini, D., and Coauthors, 2018: Uncertainty of atmospheric microwave absorption model:
504 impact on ground-based radiometer simulations and retrievals. *Atmos. Chem. Phys.*
505 *Discuss.*, <https://doi.org/10.5194/acp-2018-536>. In review.

506 De Angelis, F., and Coauthors, 2016: RTTOV-gb – adapting the fast radiative transfer model
507 RTTOV for the assimilation of ground-based microwave radiometer observations. *Geosci.*
508 *Model Dev.*, **9**, 2721–2739, <https://doi.org/10.5194/gmd-9-2721-2016>.

509 De Angelis, F., and Coauthors, 2017: Long-term observations minus background monitoring
510 of ground-based brightness temperatures from a microwave radiometer network. *Atmos.*
511 *Meas. Tech.*, **10**, 3947-3961, <https://doi.org/10.5194/amt-10-3947-2017>.

512 Fernald, F. G., B. M. Herman, and J. A. Reagan, 1972: Determination of Aerosol Height
513 Distributions by Lidar, *J. Appl. Meteorol.*, **11**, 482–489, doi:10.1175/1520-
514 0450(1972)011<0482:DOAHDB>2.0.CO;2.

515 Gryning, S.E., and Coauthors, 2016: Weibull wind-speed distribution parameters derived from
516 a combination of wind-lidar and tall-mast measurements over land, coastal and marine sites.
517 *Boundary-Layer Meteorol.*, **159**, 329–348, doi:10.1007/s10546-015-0113-x.

518 Haeffelin, M., and Coauthors, 2012: Evaluation of mixing height retrievals from automatic
519 profiling lidars and ceilometers in view of future integrated networks in Europe. *Boundary-*
520 *Layer Meteorol.*, **143**, 49–75.

521 Haeffelin, M., and Coauthors, 2016: Radiation fog formation alerts using attenuated
522 backscatter power from automatic Lidars and ceilometers. *Atmos. Meas. Tech.*, **9**, 5347-
523 5365.

524 Hervo, M., Y. Poltera, and A. Haeefe, 2016: An empirical method to correct for temperature-
525 dependent variations in the overlap function of CHM15k ceilometers. *Atmos. Meas. Tech.*,
526 **9**, 2947–2959, doi:10.5194/amt-9-2947-2016.

527 Hopkin, E, and Coauthors, 2018: A robust automated technique for operational calibration of
528 ceilometers using the integrated backscatter from totally attenuating liquid clouds.
529 Submitted to *Atmos. Meas. Tech.*

530 Illingworth, A. J., and Coauthors, 2007: Cloudnet: Continuous evaluation of cloud profiles in
531 seven operational models using ground-based observations. *Bull. Amer. Meteor. Soc.*, **88**,
532 883–898, doi:10.1175/BAMS-88-6-883.

533 Illingworth, A. J., and Coauthors, 2015: Exploiting Existing Ground-Based Remote Sensing
534 Networks to Improve High-Resolution Weather Forecasts. *Bull. Amer. Meteor. Soc.*, **96**,
535 2107-2125, doi:10.1175/BAMS-D-13-00283.1

536 Klett, J. D., 1985: Lidar Inversion with Variable Backscatter Extinction Ratios. *Appl. Opt.*, **24**,
537 1638–1643, doi: 10.1364/AO.24.001638.

538 Kotthaus, S. and C. S. B. Grimmond, 2018: Atmospheric Boundary Layer Characteristics from
539 Ceilometer measurements Part 1: A new method to track mixed layer height and classify
540 clouds. *Q. J. R. Meteorol. Soc.*, in press, doi:10.1002/qj.3299.

541 Kotthaus, S., and Coauthors, 2016: Recommendations for processing atmospheric attenuated
542 backscatter profiles from Vaisala CL31 ceilometers. *Atmos. Meas. Tech.*, **9**, 3769–3791,
543 doi:10.5194/amt-9-3769-2016.

544 Lotteraner, C., and M. Piringer, 2016: Mixing-height time series from operational ceilometer aerosol-
545 layer heights. *Boundary-Layer Meteorology*, **161**, 265-287

546 Manninen A. J., O’Connor, E. J., Vakkari, V. and T. Petäjä, 2016: A generalised background
547 correction algorithm for a Halo Doppler lidar and its application to data from Finland.
548 *Atmos. Meas. Tech.*, **9**, 817–827, doi:10.5194/amt-9-817-2016.

549 Manninen A. J., T. Marke, M. Tuononen, and E. J. O’Connor, 2018: Atmospheric boundary
550 layer classification with Doppler lidar. *J. Geophys. Res.*, Accepted for publication.
551 doi: 10.1029/2017jd028169.

552 Marke, T., and Coauthors, 2018: Long-Term Observations and High-Resolution Modeling of
553 Midlatitude Nocturnal Boundary Layer Processes Connected to Low-Level Jets. *J. Appl.*
554 *Meteor. Climatol.*, **57**, 1155–1170, <https://doi.org/10.1175/JAMC-D-17-0341.1>.

555 Martinet, P., D. and Coauthors, 2017: Combining ground-based microwave radiometer and the
556 AROME convective scale model through 1DVAR retrievals in complex terrain: an Alpine
557 valley case study. *Atmos. Meas. Tech.*, **10**, 3385-3402. [https://doi.org/10.5194/amt-10-](https://doi.org/10.5194/amt-10-3385-2017)
558 [3385-2017](https://doi.org/10.5194/amt-10-3385-2017).

559 O’Connor, E. J., A. J. Illingworth, and R. J. Hogan, 2004: A technique for autocalibration of
560 cloud lidar. *J. Atmos. Ocean. Technol.*, **21**, 777–786.

561 EJ O'Connor, E.J. and Coauthors, 2010: A method for estimating the turbulent kinetic energy
562 dissipation rate from a vertically-pointing Doppler lidar, and independent evaluation from
563 balloon-borne in-situ measurements. *J. Ocean and Atmos Tech.*, **27**, 1652-1664.

564 Päschke, E., R. Leinweber, and V. Lehmann, 2015: An assessment of the performance of a 1.5
565 μm Doppler lidar for operational vertical wind profiling based on a 1-year trial. *Atmos.*
566 *Meas. Tech.*, **8**, 2251-2266. <https://doi.org/10.5194/amt-8-2251-2015>.

567 Pattantyús-Ábrahám, M., and Coauthors, 2017: The Dataset of the CeiLinEx 2015 Ceilometer-
568 Inter-comparison Experiment, Version v001, doi 10.5676/DWD/CEILINEX2015.

569 Poltera, Y., and Coauthors, 2017: Pathfinder TURB: an automatic boundary layer algorithm.
570 Development, validation and application to study the impact on in-situ measurements at the
571 Jungfraujoch. *Atmos. Chem. Phys.*, **17**, 10051-10070.
572 <https://doi.org/10.5194/acp-17-10051-2017>.

573 Román, R., and Coauthors, 2018: Retrieval of aerosol profiles combining sun-photometer and
574 ceilometer measurements in GRASP code. *Atmospheric Research*, **204**, 161-177.

575 Rottner, L., C. Baehr, A. Dabas and L. Hammoud, 2017: Stochastic method for turbulence
576 estimation from Doppler lidar measurements. *Journal of Applied Remote Sensing* **11**(4),
577 046001. doi:10.1117/1.JRS.11.046001.

578 Rose, T., S. Crewell, U. Löhnert, and C. Simmer, 2005: A network suitable microwave
579 radiometer for operational monitoring of the cloudy atmosphere. *Atmos. Res.*, **75**, 183–
580 200, <https://doi.org/10.1016/j.atmosres.2004.12.005>.

581 Seity, Y., and Coauthors, 2011: The AROME-France convective- scale operational model,
582 *Mon. Weather Rev.*, **139**, 976–991.

583 Schween, J. H., A. Hirsikko, U. Löhnert, and S. Crewell, 2014: Mixing layer height retrieval
584 with ceilometer and Doppler lidar: from case studies to long-term assessment. *Atmos. Meas.*
585 *Tech.*, **7**, 3685-3704. <http://dx.doi.org/10.5194/amt-7-3685-2014>.

586 Suomi, I., S.-E. Gryning, E. J. O'Connor, and T. Vihma, 2017: Methodology for obtaining wind
587 gusts using Doppler lidar. *Q.J.R. Meteorol. Soc.*, **143**: 2061–2072. doi:10.1002/qj.3059.

588 Teschke, G. and V. Lehmann, 2017: Mean wind vector estimation using the velocity–azimuth
589 display (VAD) method: an explicit algebraic solution. *Atmos. Meas. Tech.*, **10**, 3265-3271.
590 <https://doi.org/10.5194/amt-10-3265-2017>.

591 Tuononen, M., E.J. O'Connor, V.A. Sinclair, and V. Vakkari, 2017: Low-Level Jets over Utö,
592 Finland, Based on Doppler Lidar Observations. *J. Appl. Meteor. Climatol.*, **56**, 2577–2594.
593 <https://doi.org/10.1175/JAMC-D-16-0411.1>.

594 Vakkari, V., E. J. O'Connor, A. Nisantzi, R. E. Mamouri, and D. G. Hadjimitsis, 2015: Low-
595 level mixing height detection in coastal locations with a scanning Doppler lidar. *Atmos.*
596 *Meas. Tech.*, **8**, 1875-1885. doi:10.5194/amt-8-1875-2015.

597 Ware, R., and Coauthors, 2003: A multichannel radiometric profiler of temperature,
598 humidity, and cloud liquid. *Radio Sci.*, **38**, 8079, <https://doi.org/10.1029/2002RS002856>,
599 2003.

600 Warren, E., and Coauthors, 2018: Evaluation of forward-modelled attenuated backscatter
601 using an urban ceilometer network in London under clear-sky conditions. *Atmos. Environ.*,
602 **191**, 532-547. doi:<https://doi.org/10.1016/j.atmosenv.2018.04.045>.

603 Westbrook, C. D., A. J. Illingworth, E. J. O'Connor, and R. J. Hogan, 2010: Doppler lidar
604 measurements of oriented planar ice crystals falling from supercooled and glaciated cloud
605 layers. *Q. J. R. Meteorol. Soc.*, **136**, 260–276. doi:10.1002/qj.528.

606 Wiegner, M. and A. Geiß, 2012: Aerosol profiling with the Jenoptik ceilometer CHM15kx.
607 *Atmos. Meas. Tech.*, **5**, 1953–1964. doi:10.5194/amt-5-1953-2012.

608 Wiegner, M., and Coauthors, 2014: What is the benefit of ceilometers for aerosol remote
609 sensing? An answer from EARLINET. *Atmos. Meas. Tech.*, **7**, 1979-1997,
610 <https://doi.org/10.5194/amt-7-1979-2014>.

611 Wiegner, M and J. Gasteiger. 2015: Correction of water vapor absorption for aerosol remote
612 sensing with ceilometers. *Atmos. Meas. Tech.*, **8**, 3971–3984. doi:10.5194/amt-8-3971-
613 2015.

614

615 **SIDEBAR: THE TOPROF COST ACTION**

616 COST or ‘European Cooperation in Science and Technology’ is a European Union funded
617 program that enables researchers to set up an interdisciplinary research networks in Europe and
618 beyond. Twenty-two European countries participated in the TOPROF action with researchers
619 from 16 National Weather Services attending together with representatives from six European
620 manufacturers of ALCs, DWLs and MWRs. Three day meetings were held twice a year each
621 with about 50 participants, but most importantly TOPROF supported 24 separate week long
622 visits by individual scientists to other research labs, national weather services, or industry,
623 where they tackled specific problems such as: changes to calibration procedures, modifications
624 to data processing that resulted in new public releases of software, physical modification of the
625 instruments and testing of forward models at national weather services. In addition, there were
626 12 special meetings to plan, execute and discuss field projects dedicated to comparing the
627 performance of different instruments with various configurations, and in some cases with
628 independent validation using instrumented towers and/or special radiosonde ascents.

629

630 **FIGURE CAPTIONS**

631 **Fig. 1.** Map of the ALC network (green - operational E-PROFILE stations: blue - stations
632 planned for 2018: red - other ceilometers reported by DWDs ceilomap). Example of E-
633 PROFILE measurements during the Saddleworth Moor fire near Manchester (26 to 27 June
634 2018). Five stations are represented: Stornoway, Eskdalemuir, Flesland, Rotterdam and
635 Ulrichstein. A photograph of the fire (courtesy E. J. O’Connor) is shown in the lower left
636 corner.

637

638 **Fig 2.** The 1064 nm attenuated backscatter for a frontal passage over Ulm, Germany on 25
639 August 2018 measured by a CHM15k ceilometer. Clouds and rain appear in black, red and
640 orange colors. Areas in green, yellow, and orange are aerosol layers. Areas above clouds where
641 the ceilometer signal is extinguished are plotted in white.

642

643 **Fig 3.** ALC measurements from eight co-located ALCs including Campbell Scientific, Vaisala,
644 and Lufft instruments based on 3 hours of data on 13 Aug 2015 during the Ceilinox campaign
645 in Lindenberg, Germany. (Left panel) raw instrument signal; (Right panel) calibrated
646 attenuated backscatter signal. 1 Mm = 10^6 m. Note the increased noise for the CL31 above 2km
647 and the divergence of the profiles below 500 m.

648

649 **Fig. 4.** Upper left panel: Attenuated Backscatter measured by the CHM15k in Valladolid
650 during a Saharan dust event from 20 to 27 June 2018. Data above clouds and with SNR lower
651 than 3 are removed. Lower left panel: Attenuated Backscatter forecast by CAMS model at the
652 closest grid point. Upper right panel: Median attenuated backscatter measured (in red) and
653 forecast (in black). Lower right panel: median of the bias between observations and forecasts.
654 Shading represents 25th and 75th percentiles.

655

656 **Fig. 5.** Three-hour time series plot generated automatically from measurements taken at
657 Charles-de-Gaulle airport (France) on 21 Jan 2016. (Top panel): fog alerts based on the method
658 of Haeffelin et al. (2016). (Lower panel): 0-400m ALC attenuated backscatter profile ($\text{m}^{-1} \text{sr}^{-1}$,
659 shown on a colored log scale) and horizontal visibility close to the surface (m, shown as a
660 gray line, the vertical axis shows the visibility on a log scale). The 1-km horizontal-visibility

661 threshold, adopted by WMO to define fog, is shown as a gray dashed line. Plots generated in
662 real-time are available at: <http://www.lmd.polytechnique.fr/~sirta/parafog/>.

663

664 **Fig. 6.** 24-hour time-height plots of Doppler lidar products generated from a Halo Photonics
665 Streamline operating in Helsinki, Finland, on 24 March 2014: (a) attenuated backscatter
666 coefficient, (b) wind speed including objective low-level jet diagnosis (black circles), (c) wind
667 direction, (d) dissipation rate of turbulent kinetic energy. The wind profiles are obtained from
668 scans at two elevations, 15 and 70 degrees from horizontal. Helsinki is situated on a coast line
669 that is aligned approximately east-west and the Doppler lidar is located about 6 km inland from
670 the coast. This combination of products illustrates the complexity of the boundary layer in a
671 coastal and urban environment, with a sea breeze driving a marine boundary layer inland
672 (northerly low-level flow from sea to land) underneath a much deeper land boundary layer
673 (more southerly flow from land to sea aloft). Solar noon is around 10 UTC, and after 1900
674 UTC all flow is from land to sea.

675

676 **Fig. 7.** One-year time series of the O–B T_B differences at Jülich (adapted from De Angelis et
677 al. 2017). From top to bottom: channels 22.24 (blue), 31.40 (red), 52.28 (magenta), and 58.00
678 GHz (cyan). Typically, RMS at zenith are within 3 K with low bias; for instrument, channel,
679 and observing angle dependencies see De Angelis et al. (2017). The black circle indicates the
680 date of a new liquid nitrogen calibration. Were such a monitoring available operationally, the
681 faulty calibration could have been detected earlier and the recalibration could have been
682 validated in near-real-time. The NWP model used here is AROME, Application of Research
683 to Operations at Mesoscale, developed by Météo-France (Seity et al., 2011).

684

685 **Fig. 8.** Profiles of RMSE with respect to radiosonde observations of the AROME NWP model

686 background (dashed) and 1DVAR updated analysis (solid) in clear (left) and cloudy (right) sky
687 conditions. During stable conditions in an enclosed alpine valley, 1DVAR assimilation of
688 MWR brightness temperatures lead to an improvement in the temperature analysis in the first
689 1500 m up to 7.5 K in clear conditions and up to ~4 K in cloudy conditions. Data from the
690 Passy-2015 field campaign (December 2014 to March 2015), Arve River valley near Passy,
691 France (Martinet et al., 2017).

692

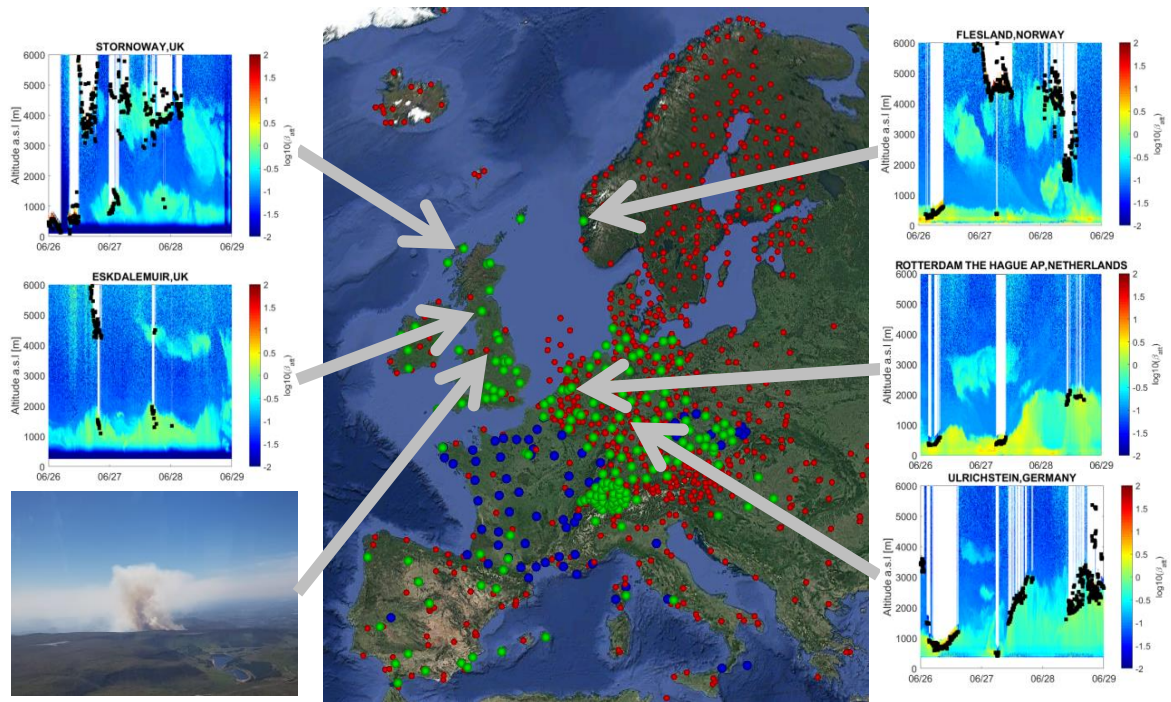
693 **Fig. 9.** 24-hour time series (28 October 2016) of temperature (top) and humidity (bottom) from
694 AROME NWP model (left), 1DVAR analysis update (center), and the difference between the
695 two (right) showing temperature increments of up to 5 K. Data from a fog field campaign at
696 Observatoire Perenne de l'Environnement (Lat: 48.56; Lon: 5.50; Alt: 388 m) near Bure
697 (France). The campaign extended from Sep 2015 to Apr 2016 and included one MWR unit.
698 NWP system is AROME 1h forecast cycle, 1.3 km horizontal resolution, 90 vertical levels.
699 The nearest grid-point 1-hour forecast is used as background for the 1DVAR retrievals at 1-
700 hour resolution, based on the closest measurements within 15 minutes.

701

702

703

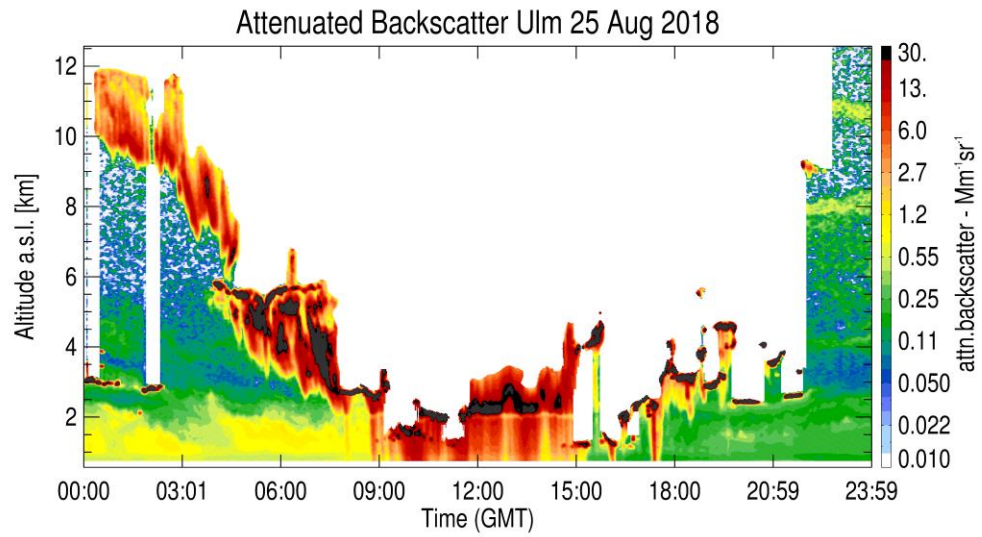
704



705
706

707 **Fig. 1.** Map of the ALC network (green - operational E-PROFILE stations: blue - stations
 708 planned for 2018: red - other ceilometers reported by DWDs ceilomap). Example of E-
 709 PROFILE measurements during the Saddleworth Moor fire near Manchester (26 to 27 June
 710 2018). Five stations are represented: Stornoway, Eskdalemuir, Flesland, Rotterdam and
 711 Ulrichstein. A photograph of the fire (courtesy E. J. O'Connor) is shown in the lower left
 712 corner.

713
714
715
716
717
718
719



720

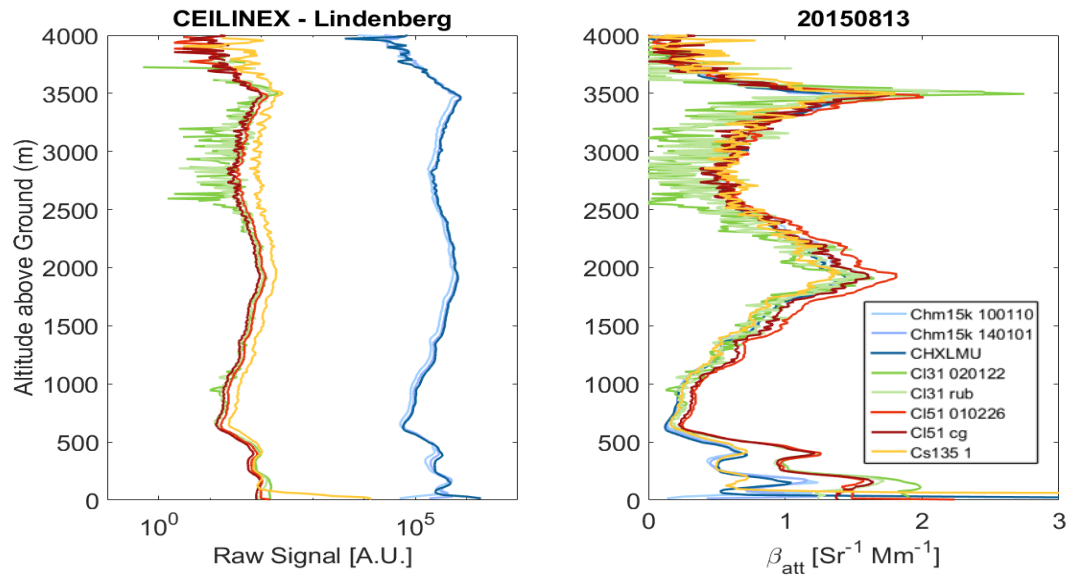
721

722 **Fig 2.** The 1064 nm attenuated backscatter for a frontal passage over Ulm, Germany on 25
 723 August 2018 measured by a CHM15k ceilometer. Clouds and rain appear in black, red and
 724 orange colors. Areas in green, yellow, and orange are aerosol layers. Areas above clouds where
 725 the ceilometer signal is extinguished are plotted in white.

726

727

728



729

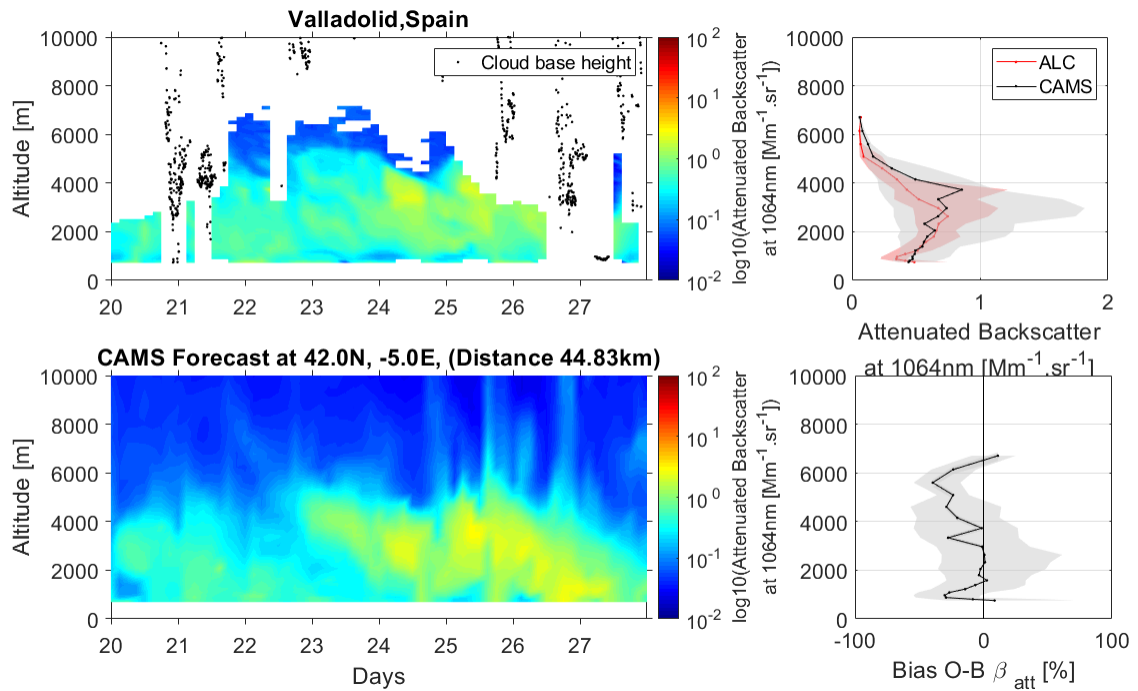
730

731 **Fig. 3** ALC measurements from eight co-located ALCs including Campbell Scientific, Vaisala,
 732 and Lufft instruments based on 3 hours of data on 13 Aug 2015 during the Ceilinox campaign
 733 in Lindenberg, Germany. (Left panel) raw instrument signal; (Right panel) calibrated
 734 attenuated backscatter signal. 1 Mm = 10^6 m. Note the increased noise for the CL31 above 2km
 735 and the divergence of the profiles below 500 m.

736

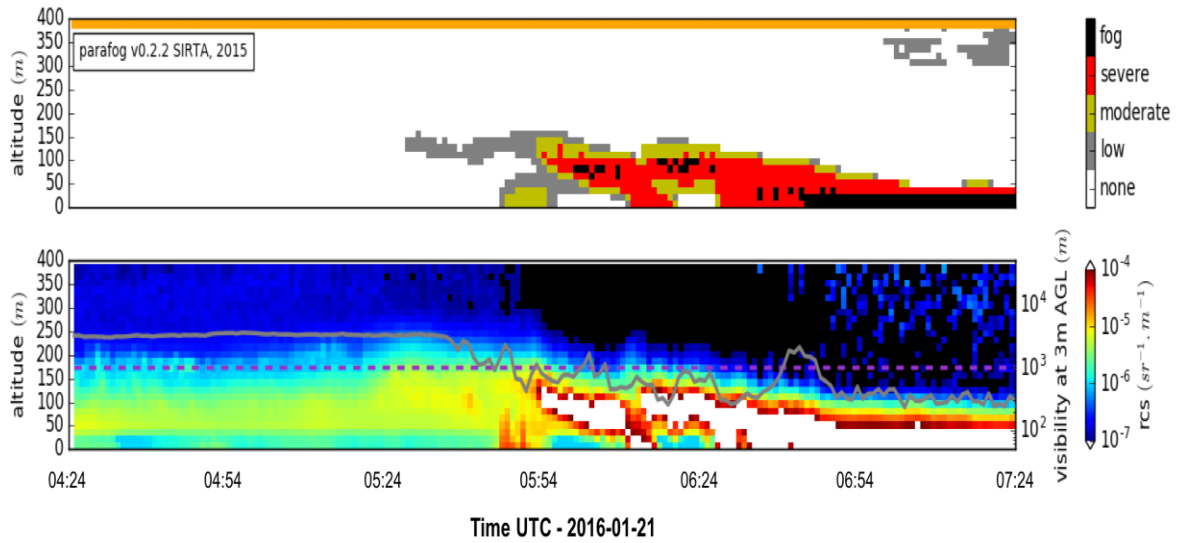
737

738



739
 740
 741
 742
 743
 744
 745
 746
 747
 748
 749
 750
 751

Fig. 4. Upper left panel: Attenuated Backscatter measured by the CHM15k in Valladolid during a Saharan dust event from 20 to 27 June 2018. Data above clouds and with SNR lower than 3 are removed. Lower left panel: Attenuated Backscatter forecast by CAMS model at the closest grid point. Upper right panel: Median attenuated backscatter measured (in red) and forecast (in black). Lower right panel: median of the bias between observations and forecasts. Shading represents 25th and 75th percentiles



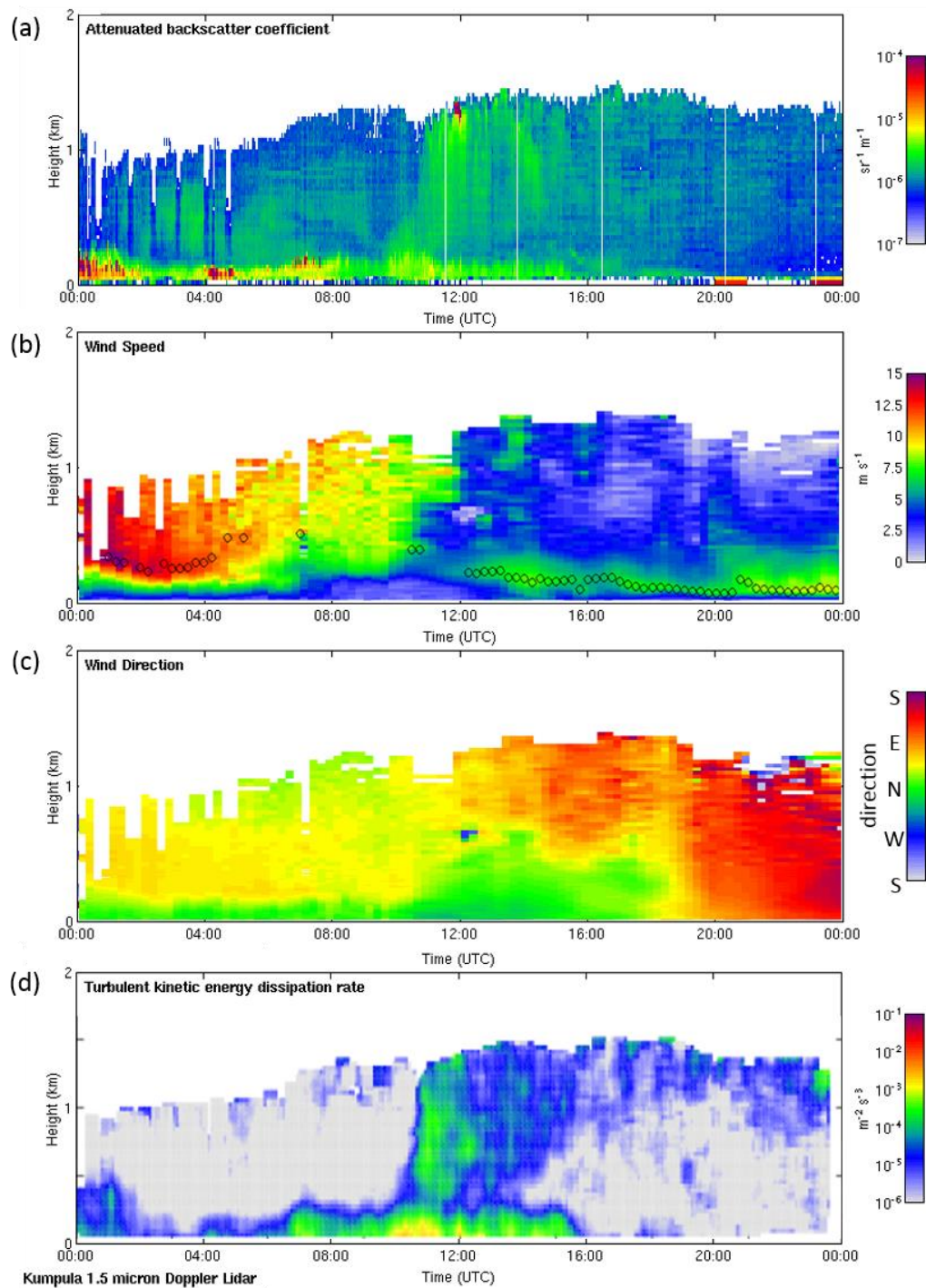
752

753

754 **Fig. 5.** Three-hour time series plot generated automatically from measurements taken at
 755 Charles-de-Gaulle airport (France) on 21 Jan 2016. (Top panel): fog alerts based on the method
 756 of Haeffelin et al. (2016). (Lower panel): 0-400 m ALC attenuated backscatter profile ($\text{m}^{-1} \text{sr}^{-1}$,
 757 shown on a colored log scale) and horizontal visibility close to the surface (m, shown as a
 758 gray line, the vertical axis shows the visibility on a log scale). The 1-km horizontal-visibility
 759 threshold, adopted by WMO to define fog, is shown as a gray dashed line. Plots generated in
 760 real-time are available at: <http://www.lmd.polytechnique.fr/~sirta/parafog/>.

761

762



763

764

765

766

767

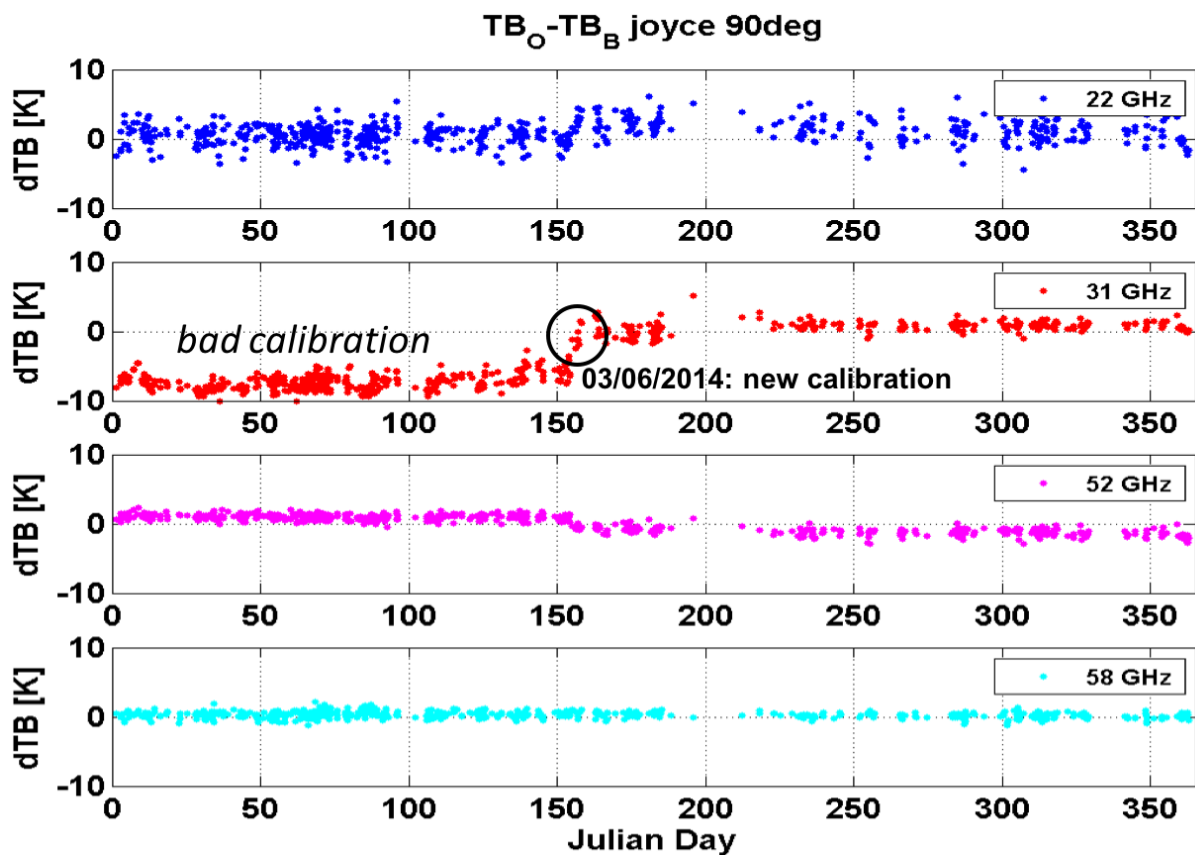
768

769

Fig. 6. 24-hour time-height plots of Doppler lidar products generated from a Halo Photonics Streamline operating in Helsinki, Finland, on 24 March 2014: (a) attenuated backscatter coefficient, (b) wind speed including objective low level jet diagnosis (black circles), (c) wind direction, (d) dissipation rate of turbulent kinetic energy. The wind profiles are obtained from scans at two elevations, 15 and 70 degrees from horizontal. Helsinki is situated on a coast line

770 that is aligned approximately east-west and the Doppler lidar is located about 6 km inland from
 771 the coast. This combination of products illustrates the complexity of the boundary layer in a
 772 coastal and urban environment, with a sea breeze driving a marine boundary layer inland
 773 (northerly low-level flow from sea to land) underneath a much deeper land boundary layer
 774 (more southerly flow from land to sea aloft). Solar noon is around 10 UTC, and after 1900
 775 UTC all flow is from land to sea.

776



777

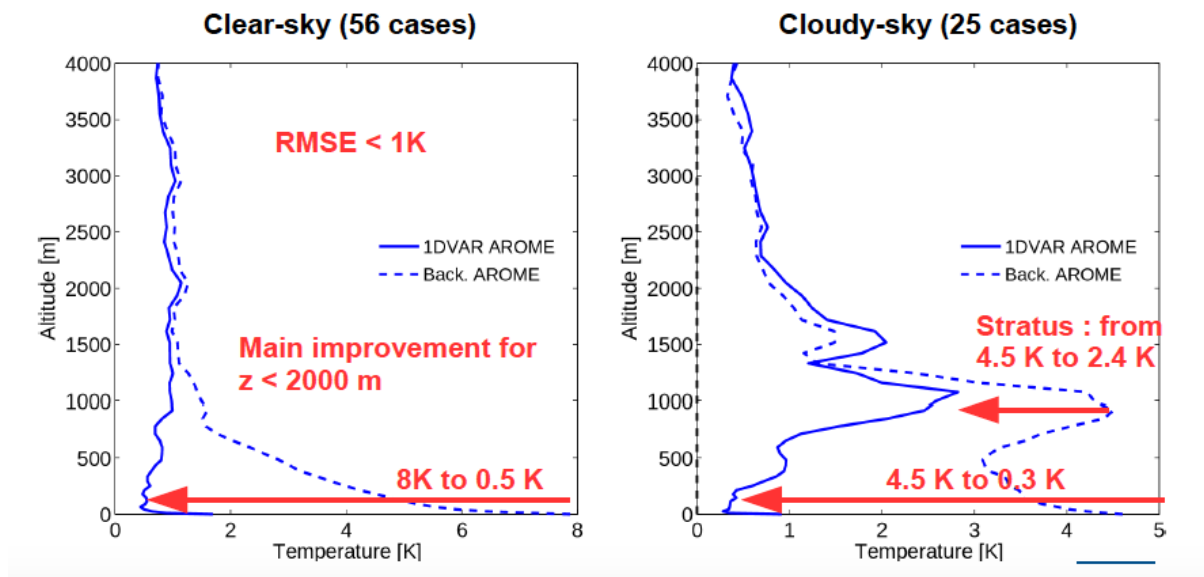
778

779 **Fig. 7.** One-year time series of the O–B T_B differences at Jülich (adapted from De Angelis et
 780 al. 2017). From top to bottom: channels 22.24 (blue), 31.40 (red), 52.28 (magenta), and 58.00
 781 GHz (cyan). Typically, RMS at zenith are within 3 K with low bias; for instrument, channel,
 782 and observing angle dependencies see De Angelis et al. (2017). The black circle indicates the
 783 date of a new liquid nitrogen calibration. Were such a monitoring available operationally, the
 784 faulty calibration could have been detected earlier and the recalibration could have been

785 validated in near-real-time. The NWP model used here is AROME, Application of Research to
786 Operations at Mesoscale, developed by Météo-France (Seity et al., 2011).

787

788



789

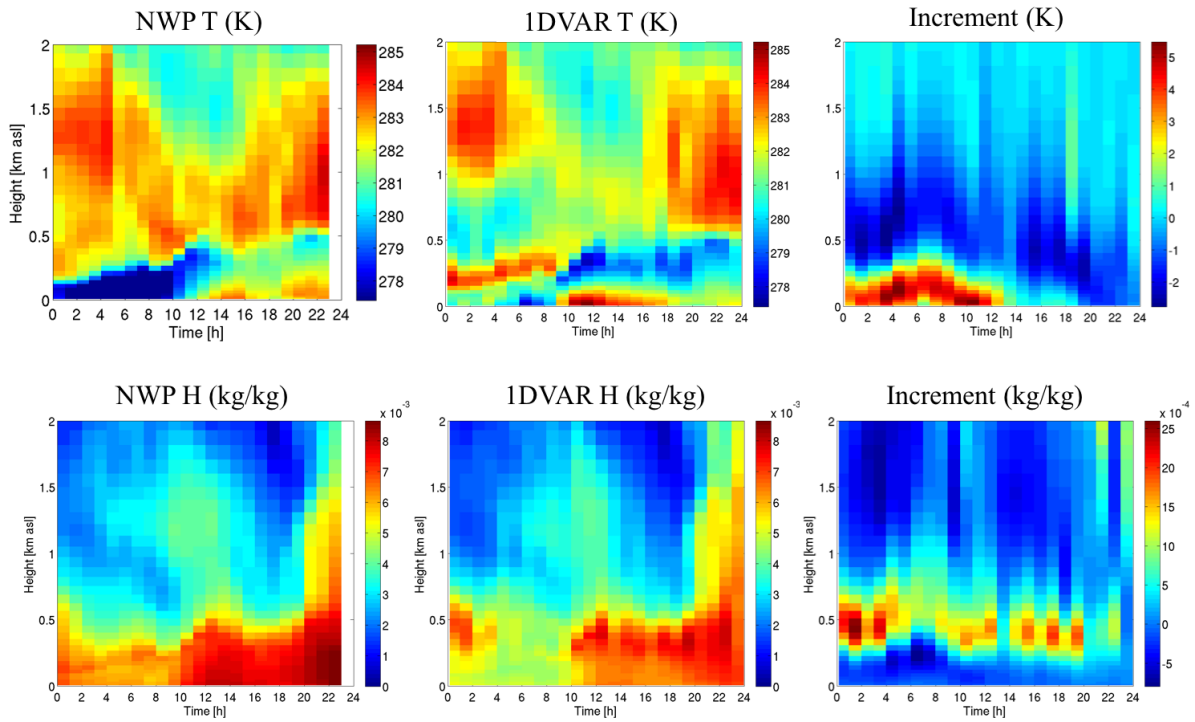
790

791 **Fig. 8.** Profiles of RMSE with respect to radiosonde observations of the AROME NWP model
792 background (dashed) and 1DVAR updated analysis (solid) in clear (left) and cloudy (right) sky
793 conditions. During stable conditions in an enclosed alpine valley, 1DVAR assimilation of
794 MWR brightness temperatures lead to an improvement in the temperature analysis in the first
795 1500 m up to 7.5 K in clear conditions and up to ~4 K in cloudy conditions. Data from the
796 Passy-2015 field campaign (December 2014 to March 2015), Arve River valley near Passy,
797 France (Martinet et al., 2017).

798

799

800



801

802

803 **Fig. 9.** 24-hour time series (28 October 2016) of temperature (top) and humidity (bottom)

804 from AROME NWP model (left), 1DVAR analysis update (center), and the difference between

805 the two (right) showing temperature increments of up to 5 K. Data from a fog field campaign

806 at Observatoire Perenne de l'Environnement (Lat: 48.56; Lon: 5.50; Alt: 388 m) near Bure

807 (France). The campaign extended from Sep 2015 to Apr 2016 and included one MWR unit.

808 NWP system is AROME 1h forecast cycle, 1.3 km horizontal resolution, 90 vertical levels.

809 The nearest grid-point 1-hour forecast is used as background for the 1DVAR retrievals at 1-

810 hour resolution, based on the closest measurements within 15 minutes.

811